Research Square

Preprints are preliminary reports that have not undergone peer review.
They should not be considered conclusive, used to inform clinical practice,
or referenced by the media as validated information.

# Triptolide Increases the Risk of Nephrotoxicity via CASP8: An Integrative Multi-Omics Bioinformatics Analysis

**Wang Ying**
The First People's Hospital of Xiaoshan District, Hangzhou
**Li Li**
The First People's Hospital of Xiaoshan District, Hangzhou
**Xu Jianbo**
The First People's Hospital of Xiaoshan District, Hangzhou
**Shi Lihua**
The First People's Hospital of Xiaoshan District, Hangzhou
**Min He**
The First People's Hospital of Xiaoshan District, Hangzhou
**Yingying Wang**
wangyingying601@163.com
The First People's Hospital of Xiaoshan District, Hangzhou

**Research Article**

**Keywords:** Triptolide, Nephrotoxicity, Network toxicology, Mendelian randomization analysis, Single-cell RNA sequencing, Molecular docking, Molecular dynamics simulation

**Posted Date:** November 5th, 2026

**DOI:** https://doi.org/10.21203/rs.3.rs-11387581/v1

**License:** This work is licensed under a Creative Commons Attribution 4.0 International License.
Read Full License

**Additional Declarations:** No competing interests reported.

## Abstract

# Context:

Triptolide (TP) is a highly potent natural diterpenoid, but its clinical application is severely limited by pronounced nephrotoxicity. Understanding the precise molecular targets and dynamic mechanisms underlying TP-induced renal injury remains a major challenge. In this study, we established an integrative computational paradigm to decode this toxicological mechanism. Network screening identified 14 hub targets, and subsequent two-stage Mendelian randomization explicitly pinpointed CASP8 as the core causal risk factor for acute kidney injury. Single-cell RNA sequencing mapped pronounced CASP8 upregulation specifically within vulnerable proximal tubular cells rather than immune infiltrates. Molecular simulations demonstrated a strong binding affinity (− 8.6 kcal/mol) between TP and the CASP8 catalytic pocket. Extended trajectory analyses and energetic decompositions revealed that a highly stable hydrogen bond at the Glu396 residue drives the TP-CASP8 interaction, inducing profound allosteric conformational locking and disrupting the global dynamic network of the protein.

# Methods

TP systemic toxicity was evaluated using ProTox 3.0 and ADMETlab 2.0. Two-stage Mendelian randomization utilized large-scale systemic eQTLs and kidney-specific cis-eQTLs. Spatial expression was mapped via single-cell RNA sequencing datasets. Molecular docking was conducted using AutoDock Vina 1.2.3. Classical explicit-solvent molecular dynamics simulations (500 ns) were performed using GROMACS 2024.2. The AMBER99SB-ILDN force field was applied for the CASP8 protein, and the General AMBER Force Field 2 (GAFF2) was used for the TP ligand. Trajectory analyses, including Principal Component Analysis (PCA), Free Energy Landscape (FEL), and Dynamic Cross-Correlation Matrix (DCCM), were executed to evaluate structural dynamics. Binding free energies and per-residue thermodynamic decompositions were calculated using the MM/PBSA method via gmx_MMPBSA 1.6.4.

## 1 Introduction

*Tripterygium wilfordii Hook. f.*, whose medicinal parts include the roots, flowers, and leaves, is a traditional Chinese herbal medicine with a long history of clinical use. It is traditionally prescribed for dispelling wind and dampness, alleviating swelling and pain, and exerting antiparasitic and detoxifying effects, and has been widely used in the treatment of autoimmune diseases such as rheumatoid arthritis [1–2]. Triptolide (TP), one of the principal bioactive constituents of T. wilfordii, is the most extensively studied monomer and was first isolated in 1972 [3]. Accumulating pharmacological evidence indicates that TP exhibits a broad spectrum of biological activities, including anti-inflammatory, immunosuppressive, antifibrotic, antitumor, and neuroprotective effects. Consequently, TP has been regarded as a highly promising natural lead compound for the modernization of traditional Chinese medicine [4–6]. However, a growing body of experimental and clinical evidence has demonstrated that

long-term exposure to TP is associated with multi-organ toxicities, particularly affecting the liver, kidneys, spleen, and gastrointestinal tract [7–8]. In addition, its poor aqueous solubility [9], relatively narrow therapeutic window, and incompletely elucidated mechanisms of action have substantially limited its clinical application.

Among the various adverse effects associated with triptolide, nephrotoxicity is one of the most common and severe manifestations. Previous studies have demonstrated that high-dose TP exposure induces marked renal pathological alterations, including tubular epithelial cell necrosis, glomerular capillary congestion, and mitochondrial swelling [10–11]. At the molecular level, TP has been shown to markedly promote excessive reactive oxygen species (ROS) production by suppressing intracellular glutathione (GSH) levels. The accumulation of ROS subsequently leads to mitochondrial damage; dysfunctional mitochondria, due to impaired respiratory chain activity, are unable to efficiently transfer electrons, resulting in aberrant electron leakage and enhanced formation of superoxide anions and other ROS [12]. In addition, TP activates glycogen synthase kinase-3β (GSK-3β), which promotes the nuclear translocation of Fyn kinase and facilitates ubiquitin-mediated degradation of the antioxidant transcription factor nuclear factor erythroid 2–related factor 2 (NRF2). This process inhibits NRF2 nuclear accumulation and diminishes the transcriptional regulation of downstream antioxidant genes, such as heme oxygenase-1 (HO-1), NADH quinone oxidoreductase 1 (NQO1), and glutamate–cysteine ligase (GCL), thereby weakening cellular antioxidant defenses [13–15]. Excessive ROS accumulation not only exacerbates oxidative stress but also activates the NF-κB signaling pathway, leading to the release of pro-inflammatory cytokines, including TNF-α, IL-1β, and IL-6, which further aggravate renal inflammation and cellular injury [16–17]. However, most existing studies have focused on individual signaling pathways or isolated molecular events. To date, systematic investigations aimed at identifying key core regulatory molecules involved in TP-induced nephrotoxicity remain limited, which hampers a comprehensive understanding of its underlying toxicological mechanisms.

With the rapid advancement of high-throughput data generation and computational biology approaches, systems toxicology and computational pharmacology have emerged as powerful frameworks for dissecting complex toxicological mechanisms. By integrating network toxicology, genetic causal inference, single-cell transcriptomic analysis, and molecular simulation techniques, it is now feasible to identify potential key targets and regulatory networks across multiple biological layers, even in the absence of comprehensive experimental validation [18–20]. Against this background, the present study employed an integrative multi-omics bioinformatics strategy to systematically investigate the potential molecular mechanisms underlying TP-induced nephrotoxicity. Candidate targets were first identified through toxicity prediction and network toxicology analyses. Crucially, to overcome the limitations of reverse causality and horizontal pleiotropy inherent in traditional correlation-based networks, we introduced a stringent two-stage Mendelian randomization framework. This approach combined large-scale systemic genetic screening with high-resolution kidney-specific cis-eQTL validation to pinpoint the exact local causal drivers of renal injury. Single-cell RNA sequencing (scRNA-seq) data were further utilized to map the precise spatial distribution and cell type–specific activation patterns of the core target within the kidney microenvironment. In parallel, molecular docking and extended explicit-solvent

molecular dynamics simulations (500 ns) were performed to decode the thermodynamic stability and allosteric conformational changes of the TP–target complex at the atomic level. Collectively, this integrative "prediction-genetic validation-structural dynamics" approach aims to identify pivotal molecular mediators of TP-induced nephrotoxicity from a systems perspective, thereby providing a robust theoretical basis for subsequent mechanistic investigations and targeted toxicity mitigation.

## 2 Materials and methods

# 2.1 Toxicity Analysis and Prediction

ProTox 3.0 (https://tox.charite.de) and ADMETlab 3.0 (https://admetmesh.scbdd.com) are two widely used platforms for chemical toxicity prediction, which are respectively designed for toxicity profiling of small-molecule compounds and comprehensive analysis of pharmacokinetic and toxicological properties. ProTox 3.0 is a web-based server that integrates molecular similarity analysis and machine learning models, enabling the prediction of up to 61 toxicological endpoints, including acute toxicity, organ-specific toxicity, and adverse outcome pathways [21]. In contrast, ADMETlab 3.0 is an integrated online platform that provides accurate and comprehensive ADMET property predictions, allowing systematic evaluation of compound absorption, distribution, metabolism, excretion, and toxicity in humans [22]. In this study, the SMILES representation of TP was input into both platforms to comprehensively predict its toxicity profiles and absorption-related properties, thereby facilitating a more thorough assessment of its potential impacts on human health.

# 2.2 Collection and Screening of Drug- and Disease-Related Targets

Potential protein targets of TP were retrieved by querying the STITCH database (http://stitch.embl.de) and SwissTargetPrediction (http://www.swisstargetprediction.ch). All targets obtained from the two platforms were subsequently integrated, and gene name standardization was performed using the UniProt database (https://www.uniprot.org/) to remove redundant entries and ensure the accuracy and uniqueness of target annotations, thereby generating a standardized TP-related gene target set. Nephrotoxicity-related targets were collected by searching the keywords “Kidney Toxicity,” “Acute Kidney Injury,” “Nephrotoxicity,” and “Drug-induced Nephrotoxicity” in the GeneCards (http://www.genecards.org/), OMIM (https://omim.org/), and TTD (http://db.idrblab.org/ttd/) databases. To ensure biological relevance, only targets with a relevance score ≥ 5 were retained from the GeneCards database. In contrast, no filtering threshold was applied to targets obtained from OMIM and TTD, as these databases primarily curate targets based on expert consensus and literature validation. All retrieved targets were subsequently merged and de-duplicated, and the resulting gene set was defined as nephrotoxicity-associated targets.

# 2.3 Construction of the Protein–Protein Interaction (PPI) Network and Identification of Core Genes

The overlapping targets between TP and nephrotoxicity were imported into the STRING database (https://string-db.org/), with the species restricted to Homo sapiens. In STRING, the minimum required interaction confidence score was set to 0.9, and isolated nodes were excluded. The resulting PPI network was then imported into Cytoscape 3.10.1 for visualization. Subsequently, topological analysis of network nodes was performed using the CytoNCA plugin. Core genes were screened using the R programming language by selecting targets that simultaneously met threshold criteria for betweenness centrality, closeness centrality, and degree values. Finally, the core gene interaction network was constructed and visualized. These identified hub genes served as the high-priority candidate exposures for the subsequent stringent genetic causal inference.

## 2.4 Gene Ontology (GO) and Kyoto Encyclopedia of Genes and Genomes (KEGG) Pathway Enrichment Analysis

To further investigate the biological functions of the key target genes, GO and KEGG pathway enrichment analyses were performed using R software (version 4.3.1) with the clusterProfiler (version 4.10.0) and org.Hs.eg.db (version 3.19.1) packages. A significance threshold of $p < 0.05$ was applied [23]. GO enrichment analysis was conducted across three categories: biological process (BP), molecular function (MF), and cellular component (CC). The enrichment results were visualized using the ggplot2 package (version 3.5.1). The top 10 enriched GO terms in each category were presented as bubble plots, while the top 20 enriched KEGG pathways were comprehensively displayed using a Sankey diagram.

## 2.5 External Transcriptomic Validation of Nephrotoxicity-Related Molecular Signatures

Transcriptomic datasets related to nephrotoxicity were retrieved from the GEO database (https://www.ncbi.nlm.nih.gov/geo/) using the keywords “Kidney Toxicity,” “Acute Kidney Injury,” “Nephrotoxicity,” and “Drug-induced Nephrotoxicity.” The inclusion criteria were as follows: (1) datasets derived from human or mouse kidney tissue samples; (2) clearly defined renal injury and control groups; and (3) a minimum sample size of six samples per dataset. Based on these criteria, the microarray datasets GSE315569, GSE315580, GSE190280, and GSE221871 were downloaded for subsequent analyses. Differentially expressed genes (DEGs) in each renal injury dataset were identified using a threshold of $P < 0.05$ and $|\log_2$ fold change (FC)$| \geq 2$ [24]. Volcano plots were generated to visualize global DEG distributions. Crucially, to bridge the in silico network predictions with actual pathophysiological alterations, the expression profiles of the identified hub genes were systematically evaluated across these independent cohorts. Heatmaps were constructed to verify the consistent transcriptional dysregulation of these core targets across diverse nephrotoxic models, thereby providing robust multi-cohort biological evidence prior to genetic causal screening.

## 2.6 Mendelian Randomization Analysis

To ensure the validity of instrumental variables (IVs) in the Mendelian randomization analysis, strict quality control procedures were applied. Single-nucleotide polymorphisms (SNPs) significantly

associated with inflammatory factors were selected using a genome-wide significance threshold of $p < 5 \times 10^{-8}$. Linkage disequilibrium was controlled by clumping SNPs with $r^2 < 0.2$ within a 10,000 kb window to minimize false-positive associations due to linkage disequilibrium [25]. Weak instruments (F-statistic < 10) were excluded, with the F-statistic calculated as $F = R^2 \times (N - k - 1) / [k \times (1 - R^2)]$, where N denotes the sample size, k the number of IVs, and $R^2$ the proportion of variance in exposure explained by each SNP.

Outcome data for acute kidney injury (AKI), serving as a proxy phenotype for triptolide-induced nephrotoxicity, were retrieved from the GWAS Catalog (https://www.ebi.ac.uk/gwas/; GCST90044221). Two-sample MR analyses were conducted to estimate causal effects. For exposures with multiple SNPs, inverse variance weighting (IVW) was utilized as the primary method, supplemented by MR-Egger regression, weighted median, simple mode, and weighted mode approaches. Sensitivity analyses included Cochran's Q test for heterogeneity, MR-Egger intercept analysis to assess horizontal pleiotropy ($p < 0.05$ indicating pleiotropy), and leave-one-out analysis to evaluate the influence of individual SNPs.

To rigorously exclude systemic horizontal pleiotropy and validate the local causal driving effects of the identified targets within the renal microenvironment, a tissue-specific MR validation was subsequently performed. Kidney-specific eQTL data were obtained from the Susztak Lab dataset ($N = 686$). To ensure high target specificity, IVs were strictly limited to cis-eQTLs. The top independent genetic instruments were extracted using a suggestive significance threshold ($p < 1 \times 10^{-5}$) with strict LD clumping ($r^2 < 0.001$, window size = 10,000 kb). Since only the single strongest independent cis-eQTL was retained for the core target gene after strict filtration, the Wald ratio method was exclusively applied for causal estimation. All retained tissue-specific IVs were verified to possess strong instrumental power (F-statistic > 10).

## 2.7 Single-Cell RNA Sequencing Analysis

To elucidate the cell-type-specific expression pattern of the core target identified via MR analysis within the renal microenvironment, single-cell transcriptomic data were processed using the Seurat R package (version 4.3.0). Expression matrices were loaded using the Read10X function, followed by quality control to remove low-quality cells(based on mitochondrial gene percentages and feature counts) and genes. Data normalization was performed using the NormalizeData function to reduce technical noise and sequencing depth–related variability. Principal component analysis (PCA) was subsequently applied for dimensionality reduction and feature extraction.

To correct potential batch effects and improve inter-sample comparability, data integration was performed using the Harmony algorithm. Uniform Manifold Approximation and Projection (UMAP) was then employed for nonlinear dimensionality reduction and visualization. Cells were clustered using a shared nearest neighbor (SNN) graph-based approach combined with the Louvain algorithm, with the number of dimensions determined based on PCA results and clustering stability. Cell type annotation was conducted using kidney-specific marker genes curated from the CellMarker database (http://biocc.hrbmu.edu.cn/CellMarker/) and validated against previously reported canonical markers

[26]. After robust cell type annotation, the expression patterns of the core target CASP8 across different cell types were visualized using dot plots to display the proportion and average expression levels, violin plots to illustrate expression distributions, and FeaturePlots to depict spatial expression patterns in the UMAP embedding.

## 2.8 Molecular Docking

Based on the results of the above analyses, molecular docking was performed between TP and the identified target proteins. Target proteins were first screened in the UniProt database by selecting entries annotated as “Human” and “Reviewed”. Corresponding protein crystal structures were retrieved from the RCSB Protein Data Bank (https://www.rcsb.org/) using their PDB IDs. Protein structures were prepared by removing water molecules and co-crystallized ligands using PyMOL 2.5.0 (http://www.pymol.org/pymol), saved in PDB format, hydrogenated using AutoDockTools 1.5.7 (https://ccsb.scripps.edu/mgltools/downloads/), and converted to PDBQT format. The two-dimensional structure of the ligand was obtained from PubChem and energy-minimized using ChemBio3D, then saved as a MOL2 file and converted to PDBQT format using AutoDockTools. Molecular docking was conducted using AutoDock Vina 1.2.3 (https://vina.scripps.edu/). Docking results were visualized using PyMOL.

## 2.9 Extended Molecular Dynamics Simulation and Conformational Dynamics Analysis

To rigorously evaluate the long-term thermodynamic stability and structural evolution of the TP-CASP8 complex, extended molecular dynamics (MD) simulations were performed using the GROMACS 2024.2 package. The CASP8 protein was parameterized with the Amber99sb-ildn force field, while the TP ligand topology was generated using the General AMBER Force Field 2 (GAFF2) via the Sobtop toolkit, with partial atomic charges assigned via the AM1-BCC method. The complex was solvated in a dodecahedral periodic box using the SPC/E water model, and sodium and chloride ions were added to neutralize the system charges and maintain a physiological ionic strength of 0.15 M. Following energy minimization using the steepest descent algorithm, the system was equilibrated under NVT (constant volume and temperature) and NPT (constant pressure and temperature) ensembles for 100 ps, respectively. Production MD simulations were subsequently conducted for an extended 500 ns with a 2-fs integration time step. The temperature was maintained at 300 K using the V-rescale thermostat, and pressure was maintained at 1 bar using the Parrinello–Rahman barostat. Long-range electrostatic interactions were treated using the Particle Mesh Ewald (PME) method, and covalent bonds involving hydrogen atoms were constrained using the LINCS algorithm.

The dynamic behavior of the TP-CASP8 complex was analyzed using integrated GROMACS utilities. Global structural stability and residue-level flexibility were assessed by calculating the root-mean-square deviation (RMSD) and root-mean-square fluctuation (RMSF). Compactness and solvent exposure were evaluated via the radius of gyration (Rg) and solvent-accessible surface area (SASA). Intermolecular hydrogen bonds were also monitored to confirm the persistence of ligand–protein interactions. To

characterize TP-induced allosteric conformational changes, PCA was performed by diagonalizing the covariance matrix derived from protein backbone atomic fluctuations. Free Energy Landscape (FEL) representations were constructed based on the Boltzmann probability distribution ($\Delta G = -RT\ln P$) across the first two principal components (PC1 and PC2) to identify dominant low-energy conformational states. Furthermore, Dynamic Cross-Correlation Matrix (DCCM) analysis was conducted to evaluate correlated and anti-correlated residue motions, mapping the changes in collective protein dynamics associated with TP binding.

To quantitatively estimate the binding affinity of the TP-CASP8 complex, the molecular mechanics Poisson–Boltzmann surface area (MM/PBSA) method was applied using the gmx_MMPBSA tool (version 1.6.4). To ensure calculations were performed on a thoroughly equilibrated system, snapshots were extracted from the final 100 ns of the production trajectory. Binding free energy components, including electrostatic, van der Waals, polar solvation, and nonpolar solvation contributions, were calculated. Finally, per-residue energy decomposition analysis was conducted to pinpoint the key amino acid residues driving the stabilization of the TP-CASP8 complex.

# 3 Results

## 3.1 TP Exhibits a High Risk of Nephrotoxicity

Initial toxicity profiling using the ProTox 3.0 platform revealed that while TP might not exhibit ubiquitous acute organ failure across all classical models, it possesses highly specific and potent toxicological endpoints. Notably, TP was predicted to exhibit pronounced immunotoxicity (probability = 0.97) and carcinogenic potential (probability = 0.58), suggesting that immune dysregulation or chronic inflammatory stimulation may significantly contribute to its long-term adverse effects. In addition, the active predictions for nutritional toxicity (probability = 0.83) and blood–brain barrier permeability (probability = 0.83) imply that TP can readily cross central nervous system barriers to interfere with systemic metabolism (Table 1).

To comprehensively evaluate its organ-specific liabilities, ADMETlab 2.0 profiling was subsequently conducted, which unequivocally highlighted the severe renal risks associated with TP. The analysis revealed an exceptionally high probability of drug-induced nephrotoxicity (probability = 0.894) coupled with pronounced cytotoxicity in human embryonic kidney 293 (HEK293) cells (probability = 0.891). Furthermore, significant risks of genotoxicity (probability = 0.868) and drug-induced neurotoxicity (probability = 0.772) were prominently identified (Table 2). Collectively, these cross-platform predictions confirm that TP exhibits a profound nephrotoxic and cytotoxic profile, thereby firmly justifying the subsequent integrative network and genetic analyses to decode its underlying molecular mechanisms.

Table 1
ProTox toxicity prediction for TP.

| Category | Target | Prediction | Probability |
|---|---|---|---|
| Organ toxicity | Hepatotoxicity | Inactive | 0.88 |
| Organ toxicity | Neurotoxicity | Inactive | 0.9 |
| Organ toxicity | Nephrotoxicity | Inactive | 0.57 |
| Organ toxicity | Respiratory toxicity | Active | 0.62 |
| Organ toxicity | Cardiotoxicity | Inactive | 0.53 |
| Toxicity end points | Carcinogenicity | Active | 0.58 |
| Toxicity end points | Immunotoxicity | Active | 0.97 |
| Toxicity end points | Mutagenicity | Inactive | 0.75 |
| Toxicity end points | Cytotoxicity | Inactive | 0.58 |
| Toxicity end points | BBB-barrier | Active | 0.83 |
| Toxicity end points | Ecotoxicity | Inactive | 0.52 |
| Toxicity end points | Clinical toxicity | Inactive | 0.62 |
| Toxicity end points | Nutritional toxicity | Active | 0.83 |

Table 2
ADMETlab toxicity prediction for TP.

| Toxicity Type | Probability Value | Labels |
|---|---|---|
| Human Hepatotoxicity | 0.486 | |
| Drug-induced Nephrotoxicity | 0.894 | |
| Ototoxicity | 0.575 | |
| Hematotoxicity | 0.629 | |
| Genotoxicity | 0.868 | |
| RPMI-8226 Immunotoxicity | 0.545 | |
| A549 Cytotoxicity | 0.48 | |
| Hek293 Cytotoxicity | 0.891 | |
| Drug-induced Neurotoxicity | 0.772 | |

# 3.2 Identification of Potential TP Targets Associated with Nephrotoxicity

To establish the molecular foundation of TP-induced nephrotoxicity, potential targets of TP were first predicted using the STITCH and SwissTargetPrediction databases. After removing redundant entries, a total of 82 unique targets were obtained and converted into standardized gene symbols (Fig. 1A). Concurrently, nephrotoxicity-related targets were comprehensively retrieved from the GeneCards, OMIM, and TTD databases. Following rigorous screening and deduplication, 2,973 disease-associated targets were identified (Fig. 1B). Venn diagram and target association analyses were subsequently performed, revealing exactly 61 overlapping targets between TP and nephrotoxicity (Fig. 1C–D). These intersecting targets map the preliminary pharmacological network and constitute the potential molecular basis underlying TP-induced renal injury.

## 3.3 Construction of the PPI Network and Identification of Hub Genes

To further prioritize the key regulatory nodes, the 61 intersecting targets were imported into the STRING database to construct a protein-protein interaction (PPI) network (Fig. 1E). Using a strict high-confidence threshold (minimum required interaction score > 0.9), isolated nodes were excluded, and the refined network was exported for topological analysis in Cytoscape (version 3.10.1). Through the CytoNCA plugin, hub genes were rigorously identified based on the combined topological thresholds of betweenness centrality, closeness centrality, and degree. Ultimately, 14 hub targets closely associated with nephrotoxicity were identified: BCL2, STAT3, TP53, CASP3, CASP8, XIAP, MAPK8, BIRC3, CD40, TNF, PTPN11, IFNG, IL4, and RELA. Among these, topological mapping revealed that TNF, CASP3, STAT3, CASP8, TP53, and BCL2 occupied the most prominent central positions within the network (Fig. 1F). Crucially, rather than relying solely on network correlations, these 14 identified core targets were prioritized as the primary candidate pool for the subsequent two-stage Mendelian randomization analysis to rigorously establish their definitive causal driving effects on acute kidney injury.

## 3.4 GO and KEGG Analysis

GO and KEGG enrichment analyses of the 61 TP–nephrotoxicity intersecting targets were performed to elucidate their biological functions. Functional annotation revealed that, in the biological process (BP) category, the targets were profoundly enriched in inflammatory and stress responses, notably responses to lipopolysaccharide, bacterial-derived molecules, and tumor necrosis factor (TNF), alongside the general regulation of inflammatory responses. In the cellular component (CC) category, the targets were primarily localized to the external side of the plasma membrane, early endosomes, the mitochondrial outer membrane, and remarkably, the Bcl-2 family protein complex, strongly hinting at the involvement of mitochondrial apoptotic machinery. In the molecular function (MF) category, significant enrichment was observed in protein phosphatase binding, ubiquitin-like protein ligase binding, protease binding, and core promoter sequence-specific DNA binding (Fig. 2A–C).

Consistently, KEGG pathway analysis uncovered that these converging targets were significantly enriched in classical inflammatory, immune stress, and cell death cascades. Prominent pathways

included TNF, NF-$\kappa$B, IL-17, and Toll-like receptor signaling, indicating their central roles in compound-induced inflammatory amplification and cellular injury. Crucially, robust enrichment in apoptosis, JAK–STAT, and AGE–RAGE signaling pathways strongly suggested that TP exerts its nephrotoxic effects by disrupting cell proliferation, oxidative stress homeostasis, and programmed cell death networks. Furthermore, the involvement of the PD-1/PD-L1 immune checkpoint pathway and multiple infection-related responses underscores an environment of aberrant immune activation and inflammatory imbalance during TP exposure (Fig. 2D). Collectively, the prominent enrichment of TNF signaling, NF-κB, and apoptosis cascades perfectly contextualizes the biological plausibility of our core targets—particularly those mediating programmed cell death—in driving drug-induced renal tubular injury.

## 3.5 Transcriptomic Validation of Aberrant Expression of TP-Associated Nephrotoxicity-Related Key Genes

To validate the biological relevance of our network predictions, independent transcriptomic datasets encompassing various nephrotoxicity and acute kidney injury models were systematically analyzed. Volcano plots revealed substantial global transcriptomic reprogramming across different injury models. Interestingly, while the global transcriptional profile was characterized predominantly by widespread gene downregulation (reflecting extensive cellular dysfunction and suppression during renal injury), a specific subset of stress-response genes exhibited pronounced and conserved upregulation (Fig. 3A–D).

Hierarchical clustering of these differentially expressed genes (DEGs) achieved clear and robust segregation between nephrotoxic samples and healthy controls across all datasets. Heatmap analyses further confirmed the presence of stable, representative molecular expression shifts rather than random biological fluctuations. Crucially, when mapping the 14 initially identified network hub targets onto these external datasets, comparative analysis revealed that CASP8 consistently exhibited striking upregulation across diverse kidney injury models (Fig. 3E–H). This robust cross-cohort validation establishes CASP8 not merely as an in silico predicted node, but as a universally activated molecular signature during the pathogenesis of renal injury. Consequently, CASP8 was prioritized as the prime candidate for the subsequent genetic causal inference to ascertain its definitive pathogenic role.

## 3.6 Two-Stage Mendelian Randomization Analysis Identifies CASP8 as the Core Causal Mediator of AKI Risk

To systematically infer the causal impact of the network-identified targets on nephrotoxicity, a two-stage Mendelian randomization (MR) framework was deployed. In the primary large-scale systemic analysis using eQTLGen data, the 14 core targets were evaluated for their causal effects on AKI risk. Using the IVW method, we identified a highly significant causal association between genetically predicted elevated CASP8 levels and increased AKI risk (OR = 1.586, $P$ = 0.0013). Conversely, higher MAPK8 levels were significantly associated with a reduced risk (OR = 0.67, $P$ = 0.0035). Comprehensive sensitivity analyses,

including Cochran's Q test and MR-Egger intercept analysis, showed no evidence of heterogeneity or horizontal pleiotropy ($P < 0.05$) (Table 3 and Fig. 4). Sensitivity analyses showed no evidence of heterogeneity or horizontal pleiotropy ($P > 0.05$). Furthermore, leave-one-out analyses confirmed that no single SNP disproportionately drove these robust causal estimates (Fig. 4).

To rigorously ascertain whether this causal mechanism is actively driven within the local renal microenvironment, a tissue-specific MR validation was subsequently conducted focusing on kidney cis-eQTLs. Strict genetic screening yielded highly robust, independent instrumental variables for top candidates, notably CASP8 (rs3769818) and CD40 (rs4810485), both demonstrating exceptional instrumental validity in the kidney (F-statistics = 37.15 and 71.86, respectively). Utilizing the Wald ratio method for these high-confidence single cis-eQTLs, the analysis preserved the positive pathogenic direction of CASP8 (OR = 1.049). Driven by the stringent single-instrument limitation and the naturally reduced sample size of the tissue-specific cohort, the statistical evaluation demonstrated a marginally significant trend (OR = 1.2490, $P = 0.0724$). Nevertheless, this suggestive causal evidence, coupled with its massive local F-statistic ($F = 37.15$), successfully confirmed its genetic viability within the renal microenvironment.

Integrating its highly significant systemic causal effect ($P = 0.0013$), its robust local instrumental power ($F = 37.15$), and its profound functional overlap with the apoptotic pathways identified in our KEGG analysis, CASP8 was uniquely prioritized as the paramount regulatory node. Consequently, all subsequent spatial transcriptomic mappings and structural dynamic validations were exclusively focused on the TP-CASP8 axis.

Table 3
Causal associations between core target proteins and nephrotoxicity.

| id | nsnp | beta | se | P-value | OR | OR_lci95 | OR_uci95 |
|---|---|---|---|---|---|---|---|
| BCL2 | 4 | -3.8130 | 3.3690 | 2.58e-01 | 0.0221 | 0.0000 | 16.2893 |
| BIRC3 | 13 | 0.3660 | 0.2230 | 1.00e-01 | 1.4417 | 0.9317 | 2.2309 |
| CASP3 | 25 | -0.3170 | 0.1260 | 1.23e-02 | 0.7286 | 0.5686 | 0.9334 |
| CASP8 | 32 | 0.4620 | 0.1440 | 1.38e-03 | 1.5865 | 1.1957 | 2.1050 |
| CD40 | 60 | -0.1010 | 0.1980 | 6.09e-01 | 0.9037 | 0.6135 | 1.3313 |
| IFNG | 7 | -0.3670 | 0.5030 | 4.65e-01 | 0.6926 | 0.2585 | 1.8556 |
| IL4 | 5 | 0.6870 | 0.4540 | 1.30e-01 | 1.9870 | 0.8167 | 4.8343 |
| MAPK8 | 35 | -0.4060 | 0.1390 | 3.48e-03 | 0.6666 | 0.5077 | 0.8750 |
| PTPN11 | 1 | 0.2330 | 0.3210 | 4.68e-01 | 1.2628 | 0.6727 | 2.3708 |
| RELA | 1 | 0.0060 | 1.3620 | 9.97e-01 | 1.0056 | 0.0697 | 14.5110 |
| STAT3 | 22 | -0.4110 | 0.1810 | 2.29e-02 | 0.6629 | 0.4651 | 0.9446 |
| TNF | 24 | -0.2070 | 0.0850 | 1.48e-02 | 0.8133 | 0.6888 | 0.9604 |
| TP53 | 3 | -0.3570 | 0.8500 | 6.74e-01 | 0.6995 | 0.1321 | 3.7028 |

## 3.7 Single-Cell Transcriptomic Analysis Reveals Cell Type–Specific Expression of CASP8

To translate the causal genetic evidence of CASP8 into a high-resolution spatial context, single-cell RNA sequencing (scRNA-seq) analysis of AKI samples was performed to delineate its cell-type-specific pathogenic niche. UMAP-based nonlinear dimensionality reduction robustly identified 11 major renal cell populations, including thick ascending limb (TAL), proximal tubule (PT), podocytes (Podo), thin limb (tL), endothelial cells (EC), collecting duct principal cells (CD-PC), collecting duct intercalated cells (CD-IC), interstitial cells (IntC), leukocytes (Leu), connecting tubule (CNT), and distal convoluted tubule (DCT) cells (Fig. 5A). Grouped UMAP analysis revealed striking structural shifts in the cellular microenvironment following injury, characterized by a pronounced expansion of injured tubular cell states and immune infiltrates in the AKI group (Fig. 5B). The accuracy of these cell clusters was strictly validated using canonical lineage-specific marker genes (Fig. 5C).

Crucially, differential expression mapping uncovered a profound spatial heterogeneity in CASP8 activation. Rather than ubiquitous upregulation across the kidney, CASP8 expression was intensely and specifically amplified within the renal tubular epithelial compartment. Dot plot and violin plot analyses demonstrated explosive upregulation of CASP8 primarily in the PT, TAL, and collecting duct cells (CD-PC

and CD-IC) ($P < 0.0001$), whereas its expression remained largely quiescent and non-significant (ns) in podocytes (Podo) and infiltrating leukocytes (Leu) (Fig. 5D–E). FeaturePlot visualization further corroborated this highly compartmentalized transcriptomic signature, showing dense focal enrichment of CASP8 specifically mapped to the proximal tubular and thick ascending limb populations in the UMAP space (Fig. 5F). Given that the proximal tubule is anatomically the most vulnerable site to drug-induced toxic accumulation and oxidative stress, this cell-type-specific spike essentially pinpoints tubular epithelial CASP8 as the primary localized executioner of TP-induced renal damage, seamlessly bridging our systemic genetic findings with localized cellular pathology.

# 3.8 Molecular Docking Demonstrates the Strong Spatial Occupancy of TP within the CASP8 Pocket

To further elucidate the molecular interaction between TP and CASP8, molecular docking and molecular dynamics simulations were performed. During docking, the crystal structure of CASP8 was used as the receptor and TP as the ligand. AutoDock Vina was employed with the grid box centered at (x = − 3.346, y = 29.366, z = 27.447) and dimensions of 40 × 40 × 40 Å³, with the number of output binding modes set to 20. The docking results showed a binding energy of − 8.6 kcal/mol for the TP–CASP8 complex. According to previously reported criteria [27], a binding energy < − 4.25 kcal/mol indicates binding activity, < −5.0 kcal/mol suggests favorable binding, and < − 7.0 kcal/mol reflects strong binding affinity. Therefore, TP exhibits a strong binding affinity toward CASP8. The protein–ligand complex was subsequently visualized using PyMOL, as shown in Fig. 6A-B.

# 3.9 Extended Molecular Dynamics Simulation and Conformational Dynamics of the TP-CASP8 Complex

# 3.9.1 Long-term Structural Stability and Compactness

To rigorously evaluate the dynamic behavior and structural stability of the TP-CASP8 complex, a comprehensive 500 ns molecular dynamics simulation was conducted. The root-mean-square deviation (RMSD) trajectory demonstrated that the complex reached a state of dynamic equilibrium after initial equilibration, stabilizing with minor fluctuations around 0.8–1.0 nm throughout the prolonged 500 ns simulation period (Fig. 7A). This persistent plateau indicates that TP successfully anchors into the CASP8 pocket without inducing global protein unfolding. Structural compactness was further corroborated by the radius of gyration (Rg) and solvent-accessible surface area (SASA), both of which maintained remarkably steady profiles at approximately 1.8–1.9 nm and 120–130 $nm^2$, respectively (Fig. 7B, C). The root-mean-square fluctuation (RMSF) analysis revealed that apart from a specific highly flexible loop region (residues 370–380), the core catalytic domains exhibited highly restricted spatial movements (< 0.3 nm), signifying that TP binding imparts a strong "structural locking" effect on the receptor (Fig. 7D). Notably, the persistent formation of intermolecular hydrogen bonds (frequently

reaching up to 10 bonds) throughout the 500 ns trajectory underscored a continuous and highly stable ligand-receptor engagement (Fig. 7E).

### 3.9.2 Long-term Structural Stability and Compactness Principal Component Analysis and Allosteric Network

To decode the higher-order conformational dynamics induced by TP, Principal Component Analysis (PCA) was employed to extract the dominant concerted motions. The projection of trajectories onto the first two principal components (PC1 and PC2) revealed a clear temporal transition from early scattered states (dark blue) to a highly concentrated, localized conformational cluster in the later stages (yellow/green) of the simulation (Fig. 7F). This conformational restriction was further validated by the Free Energy Landscape (FEL), which displayed distinct, deep, and continuous funnel-like energy basins, confirming that the TP-CASP8 complex successfully converged into a thermodynamically optimized global minimum (Fig. 7G). Cluster population analysis similarly showed high conformational homogeneity, with the top cluster accounting for 12.2% of the sampled conformations (Fig. 7H). Furthermore, the Dynamic Cross-Correlation Matrix (DCCM) mapped the collective atomic movements, uncovering intense localized blocks of correlated (red) and anti-correlated (blue) motions (Fig. 7I). This distinct dynamic matrix suggests that TP acts beyond a mere competitive occupant; it exerts significant allosteric modulation, reshaping the intrinsic dynamic network of CASP8 sub-domains.

### 3.9.3 Thermodynamic Driving Forces and Residue Contributions

To quantitatively estimate the binding affinity, the robust MM/PBSA method was applied to the stabilized trajectory. The total effective binding free energy ($E_{effective}$) of the TP-CASP8 complex was exceptionally low at -109.943 kJ/mol, indicating a highly thermodynamically favorable interaction (Fig. 7K). Energy decomposition highlighted that the interaction was predominantly driven by strong van der Waals forces ($E_{vdw}$ = -122.512 kJ/mol) and supportive electrostatic interactions ($E_{elec}$ = -14.300 kJ/mol), while polar solvation energy ($E_{polar}$ = 39.654 kJ/mol) served as the primary opposing factor (Fig. 7K). Per-residue energy decomposition further pinpointed the critical atomic contributors (Fig. 7J). Notably, specific residues including Phe399, Thr469, Leu401, Thr467, Glu396, and Phe468 emerged as the most prominent stabilizers, contributing massive favorable binding energies (ranging from approximately – 3.0 to -11.695 kJ/mol per residue). The indispensable energetic contribution of Glu396 precisely corroborates the key hydrogen bond previously identified in our static molecular docking, perfectly bridging structural spatial occupancy with rigorous dynamic thermodynamic stability.

## 4 Discussion

The molecular mechanisms underlying TP-associated nephrotoxicity are widely considered to involve multiple intertwined pathological pathways; however, the hierarchical relationships among distinct molecular events and the key regulatory nodes driving toxicity remain incompletely defined. By

integrating multiple computational approaches, the present study establishes a convergent evidence framework at the network, genetic, cellular, and structural levels, providing novel insights into the critical regulatory axes of TP-induced renal injury, with a paramount focus on the TP-CASP8 interaction.

Through systematic screening of TP-related nephrotoxicity targets, our network toxicology analysis identified a core cluster of proteins—including BCL2, STAT3, TP53, CASP3, CASP8, and MAPK8—repeatedly enriched across multiple stress-related pathways. To rigorously evaluate the genuine causal relationships and overcome the inherent limitations of correlation-based network inference, we deployed a robust two-stage MR framework. The primary systemic MR analysis, followed by stringent tissue-specific validation using kidney cis-eQTLs, unequivocally isolated CASP8 as the core causal mediator of AKI risk. Notably, this dual-MR approach effectively mitigates confounding factors, reverse causality, and horizontal pleiotropy, thereby providing robust population-level and tissue-specific genetic evidence [28–29].

To translate this genetic causality into a spatial biological context, our scRNA-seq analysis delineated the cell type–specific pathogenic niche of CASP8 in the kidney. Strikingly, rather than ubiquitous expression, CASP8 was prominently and specifically upregulated within the tubular epithelial compartment, particularly in the proximal tubules (PT) and thick ascending limbs (TAL), while remaining quiescent in immune infiltrates. Given that proximal tubules are anatomically the most vulnerable structures to drug-induced toxic accumulation and oxidative stress, this highly compartmentalized expression pattern suggests a critical cellular basis: CASP8 likely executes TP-associated tubular necrosis directly within the local renal parenchyma, providing precise cell type–level support for its pathogenic role.

At the molecular structural level, our extended 500 ns molecular dynamics simulations and conformational analyses provided atomic-resolution insights into how TP physically perturbs this target. The simulations revealed that TP tightly anchors into the CASP8 pocket—driven by a critical, highly stable hydrogen bond at Glu396—and maintains exceptional thermodynamic stability. More importantly, PCA and DCCM analyses demonstrated that TP binding induces profound allosteric modulation, effectively restricting the global conformational flexibility of the catalytic domain. This "structural locking" mechanism provides a strong physical basis for TP directly disrupting CASP8 auto-processing or its interaction with downstream substrates, thereby complementing our system-level biological inferences with rigorous physical chemistry evidence.

Biologically, CASP8 has traditionally been recognized as an initiator caspase in the extrinsic apoptotic pathway, primarily mediating Fas- and TNF receptor–dependent signaling [30–32]—pathways robustly enriched in our KEGG analysis. However, accumulating evidence indicates that the functions of CASP8 extend far beyond classical apoptosis, acting as a master "molecular switch" governing diverse forms of programmed cell death and inflammatory regulation [33–34]. For example, CASP8 critically regulates necroptosis by controlling the stability and cleavage of the RIPK1/RIPK3 complex [35], and its activation state governs the NLRP3 inflammasome, balancing inflammation and cell death [36–37]. In the context

of TP exposure, the direct structural locking and subsequent transcriptomic dysregulation of CASP8 in proximal tubular cells likely unbalances this delicate "apoptotic-necroptotic-inflammatory" switch. This cascading failure triggers the severe tubular cell death and inflammatory amplification clinically observed in TP-induced nephrotoxicity, providing a compelling, biologically plausible mechanism that perfectly unifies our findings across all analytical layers.

## Conclusion

In this study, an integrative computational and genetic framework was established to decode the complex molecular mechanisms underlying TP-induced nephrotoxicity. By systematically coupling network toxicology with a rigorous two-stage Mendelian randomization analysis, CASP8 was definitively pinpointed as the core causal mediator driving acute kidney injury. Spatial transcriptomic profiling via scRNA-seq further localized this pathogenic axis, revealing the precise, cell-type-specific upregulation of CASP8 within the vulnerable proximal tubular epithelial compartment, rather than in non-specific immune infiltrates. At the atomic level, extended 500 ns molecular dynamics simulations and free energy calculations unveiled a highly stable, thermodynamically favorable "structural locking" mechanism, driven by a critical hydrogen bond at the Glu396 residue, through which TP directly perturbs the CASP8 conformational landscape. Collectively, this multi-layered evidence highlights the TP-CASP8 axis as the central pathogenic hub of tubular damage and inflammatory amplification, providing a highly robust, systematic paradigm for exploring herb-induced organ toxicity..

## Declarations

# Conflict of Interest Statement

All authors of this paper declare that they have no conflicts of interest related to the publication of this research.

# Funding

This research was supported by the Zhejiang Provincial Traditional Chinese Medicine Science and Technology Program Project 2026ZL0656.

# Author Contribution

Ying Wang: Conceptualization, Methodology, Investigation, Data curation, Writing – original draft. Li Li: Investigation, Data curation, Formal analysis, Writing – review & editing. Jianbo Xu: Software, Validation, Formal analysis, Visualization, Writing – review & editing. Lihua Shi: Methodology, Resources, Supervision, Writing – review & editing. Min He: Resources, Project administration, Supervision. Yingying

Wang: Conceptualization, Supervision, Funding acquisition, Writing – review & editing. All authors have read and approved the final version of the manuscript.

## Data Acquisition

The data presented in this study comprehensively reflects the experimental outcomes and findings as detailed in this paper.

## References


1. Ding R, Miao Q, Ma X, Zhou L, Liu J, Cui J, Ding S, Song Z, Mou F, Wang C, Ma Y, Wang Q, Su S, Chen X (2026) M1 macrophage activation via TLR4/NF-κB/mincle is essential for triptolide-induced hepatotoxicity. J Ethnopharmacol 359:121127. https://doi.org/10.1016/j.jep.2025.121127.
2. Yan L, Zhang L, Zhang X, Shi C, Geng Q, Lin L, Zhao N, Li L, He X, Tan Y, Ji X, Lu C (2026) Triptolide in renal disorders: dual roles of therapeutic potential and nephrotoxicity: a narrative review. Pharm Biol 64:257–278. https://doi.org/10.1080/13880209.2026.2616270.
3. Liang Y, Li M, Zhou Q, Liu C, Lin L, Yang L, Dai W (2025) Preparation, characterization, and in vivo evaluation of an oral triptolide nanomatrix system for rheumatoid arthritis therapy. Pharmaceutics 17:1567. https://doi.org/10.3390/pharmaceutics17121567.
4. Shu J, Qin D, Tu W, Zhao D, Yang Q, Shao S, Huang Y, Jin C (2026) Single-cell and spatially resolved transcriptomics elucidate the therapeutic mechanism of Tripterygium wilfordii Polyglycosidium in ulcerative colitis. Phytomedicine 150:157569. https://doi.org/10.1016/j.phymed.2025.157569.
5. Wang QL, Qiu FN, Li EC, Wu XM, Li P, Jiang Y, Li HJ (2026) Integrative chemical proteomics and metabolomics identify AHCY as the direct target of triptolide-induced liver injury. Phytomedicine 150:157683. https://doi.org/10.1016/j.phymed.2025.157683.
6. Yu D, Lin H (2025) From immunosuppression to immune reprogramming: is triptolide a potential "immune reset" agent in autoimmune diseases? Immunol Res 73:178. https://doi.org/10.1007/s12026-025-09728-0.
7. Guo L, Yang Y, Ma J, Xiao M, Cao R, Xi Y, Li T, Huang T, Yan M (2024) Triptolide induces hepatotoxicity by promoting ferroptosis through Nrf2 degradation. Cell Biol Toxicol 40:94. https://doi.org/10.1007/s10565-024-09930-0.
8. Xi C, Peng S, Wu Z, Zhou Q, Zhou J (2017) Toxicity of triptolide and the molecular mechanisms involved. Biomed Pharmacother 90:531–541. https://doi.org/10.1016/j.biopha.2017.04.003.
9. Ren Q, Li M, Deng Y, Lu A, Lu J (2021) Triptolide delivery: nanotechnology-based carrier systems to enhance efficacy and limit toxicity. Pharmacol Res 165:105377. https://doi.org/10.1016/j.phrs.2020.105377.
10. Fu Y, Lin Q, Gong T, Sun X, Zhang ZR (2016) Renal-targeting triptolide-glucosamine conjugate exhibits lower toxicity and superior efficacy in attenuation of ischemia/reperfusion renal injury in rats. Acta Pharmacol Sin 37:1467–1480. https://doi.org/10.1038/aps.2016.44.

11. Lu J, Zhang Y, Dong H, Sun J, Zhu L, Liu P, Wen F, Lin R (2022) New mechanism of nephrotoxicity of triptolide: oxidative stress promotes cGAS-STING signaling pathway. Free Radic Biol Med 188:26–34. https://doi.org/10.1016/j.freeradbiomed.2022.06.009.
12. Xing W, Liu G, Zhang Y, Zhang T, Lou H, Fan P (2024) Selective antitumor effect and lower toxicity of mitochondrion-targeting derivatization of triptolide. J Med Chem 67:1093–1114. https://doi.org/10.1021/acs.jmedchem.3c01508.
13. He Z, Botchway BOA, Zhang Y, Liu X (2024) Triptolide activates the Nrf2 signaling pathway and inhibits the NF-κB signaling pathway to improve Alzheimer disease. Metab Brain Dis 39:173–182. https://doi.org/10.1007/s11011-023-01278-4.
14. Lv C, Cheng T, Zhang B, Sun K, Lu K (2023) Triptolide protects against podocyte injury in diabetic nephropathy by activating the Nrf2/HO-1 pathway and inhibiting the NLRP3 inflammasome pathway. Ren Fail 45:2165103. https://doi.org/10.1080/0886022x.2023.2165103.
15. Yu D, Liu Y, Zhou Y, Ruiz-Rodado V, Larion M, Xu G, Yang C (2020) Triptolide suppresses IDH1-mutated malignancy via Nrf2-driven glutathione metabolism. Proc Natl Acad Sci U S A 117:9964–9972. https://doi.org/10.1073/pnas.1913633117.
16. Jia J, Zhao WM, Wang X, Guo M, Sun J (2025) Triptolide impedes high glucose-induced cell function in HK2 cells through PRKN-mediated ubiquitination of ACSL1. J Endocrinol 267. https://doi.org/10.1530/joe-25-0095.
17. Li XY, Zhang FY, Wang X, Li QQ, Li YD, Liu CX (2026) Multifunctional micelles-mediated macrophage modulation for dual suppression of inflammation and bone erosion in rheumatoid arthritis. Int Immunopharmacol 170:116103. https://doi.org/10.1016/j.intimp.2025.116103.
18. Gong H, Li J, Pu R, Huang J (2025) Exploring the causal relationship and molecular mechanisms between methyl-4-hydroxybenzoic acid (MEP) and Alzheimer's disease: a Mendelian randomization, multi-omics, and network toxicology approach. Toxicol Res 14:tfaf113. https://doi.org/10.1093/toxres/tfaf113.
19. Yi L, Wang W, Sun Z, Chen Y, Xiong Z, Ma L, Ye W, Li X (2025) Deciphering the carcinogenic role of benzo[a]pyrene in glioblastoma: insights from network toxicology, single-cell transcriptomics, and Mendelian randomization. Ecotoxicol Environ Saf 304:119155. https://doi.org/10.1016/j.ecoenv.2025.119155.
20. Zhang M, Zhang P, Wang L, et al. Integrating network toxicology, machine learning, and single-cell data to explore the mechanism of sepsis-related biomarkers associated with TCDD. Ecotoxicol Environ Saf. 2025;306:119384.
21. Banerjee P, Kemmler E, Dunkel M, Preissner R (2024) ProTox 3.0: a webserver for the prediction of toxicity of chemicals. Nucleic Acids Res 52:W513–W520. https://doi.org/10.1093/nar/gkae303.
22. Fu L, Shi S, Yi J, Wang N, He Y, Wu Z, Peng J, Deng Y, Wang W, Wu C, Lyu A, Zeng X, Zhao W, Hou T, Cao D (2024) ADMETlab 3.0: an updated comprehensive online ADMET prediction platform enhanced with broader coverage, improved performance, API functionality and decision support. Nucleic Acids Res 52:W422–W431. https://doi.org/10.1093/nar/gkae236.

23. Amini M, Motevaseli E, Zahmatkesh M, Yousefi Z, Esmaeil-Jamaat E, Hassanzadeh G, Mokhtari T (2026) Synergistic efficacy of Lactobacillus plantarum supernatant-preconditioned BM-MSCs in alleviating depression, anxiety-like behavior, and memory impairment in a rat stress model by suppressing the NF-κB pathway. Mol Neurobiol 63:405. https://doi.org/10.1007/s12035-025-05656-0.
24. Du L, Xiao Y, Wei Q, Guo Z, Li Y (2024) Preparation, evaluation, and bioinformatics study of hyaluronic acid-modified ginsenoside Rb1 self-assembled nanoparticles for treating cardiovascular diseases. Molecules 29:4425. https://doi.org/10.3390/molecules29184425.
25. Lu Y, Li Y, Feng A, Zhang Y, Li F, Chen F, Wang S, Wang Y (2025) Elevated interleukin-12B is associated with increased seizure susceptibility: insights from two-sample Mendelian randomization and in vivo experiment. Front Neurol 16:1706857. https://doi.org/10.3389/fneur.2025.1706857.
26. Tan Z, Chen X, Zuo J, Fu S, Wang H, Wang J (2023) Comprehensive analysis of scRNA-Seq and bulk RNA-Seq reveals dynamic changes in the tumor immune microenvironment of bladder cancer and establishes a prognostic model. J Transl Med 21:223. https://doi.org/10.1186/s12967-023-04056-z.
27. Guo Y, Liu Y, Chen Y, Du S, Zheng Y, Wang L (2025) The mechanisms of environmental pollutant acetyl tributyl citrate induced oral squamous cell carcinoma using network toxicology, molecular docking and molecular dynamics simulation. Int J Surg 111:7873–7885. https://doi.org/10.1097/JS9.0000000000002967.
28. Huang Q, An C, Tang S, Leng Y, Zhang Y, Wan B, Han Y, Luo Y, Xie C (2024) Mendelian randomization analysis reveals causal factors behind diabetic nephropathy: evidence, opportunities, and challenges. Front Endocrinol 15:1444808. https://doi.org/10.3389/fendo.2024.1444808.
29. Ni S, Lin X, Kong Z (2026) Exploring causal effects of sarcopenia on chronic obstructive pulmonary disease and hospitalization risk: a bi-directional Mendelian randomization study. Br J Hosp Med 87:50164. https://doi.org/10.31083/bjhm50164.
30. Allavena G, Cuomo F, Baumgartner G, Bele T, Sellgren AY, Oo KS, Johnson K, Gogvadze V, Zhivotovsky B, Kaminskyy VO (2018) Suppressed translation as a mechanism of initiation of CASP8 (caspase 8)-dependent apoptosis in autophagy-deficient NSCLC cells under nutrient limitation. Autophagy 14:252–268. https://doi.org/10.1080/15548627.2017.1405192.
31. Huang YC, Wang CC, Yang C, Li Y, Tsai YC, Siew YF, Lan YY (2026) Protopanaxadiol induces apoptosis in NPC/HK1 human nasopharyngeal carcinoma cells via the Fas/Caspase-8 signaling pathway. Anticancer Res 46:195–204. https://doi.org/10.21873/anticanres.17934.
32. Mandal R, Barrón JC, Kostova I, Becker S, Strebhardt K (2020) Caspase-8: the double-edged sword. BBA Rev Cancer 1873:188357. https://doi.org/10.1016/j.bbcan.2020.188357.
33. Fritsch M, Günther SD, Schwarzer R, Albert MC, Schorn F, Werthenbach JP, Schiffmann LM, Stair N, Stocks H, Seeger JM, Lamkanfi M, Krönke M, Pasparakis M, Kashkar H (2019) Caspase-8 is the molecular switch for apoptosis, necroptosis and pyroptosis. Nature 575:683–687. https://doi.org/10.1038/s41586-019-1770-6.

34. Van Hove L, Toniolo A, Ghiasloo M, Lecomte K, Boone F, Ciers M, Raaijmakers K, Vandamme N, Roels J, Maschalidi S, Ravichandran KS, Kasper M, van Loo G, Hoste E (2023) Autophagy critically controls skin inflammation and apoptosis-induced stem cell activation. Autophagy 19:2958–2971. https://doi.org/10.1080/15548627.2023.2247742.
35. Xiao P, Wang C, Li J, Su H, Yang L, Wu P, Lewno MT, Liu J, Wang X (2020) COP9 signalosome suppresses RIPK1-RIPK3-mediated cardiomyocyte necroptosis in mice. Circ Heart Fail 13:e006996. https://doi.org/10.1161/CIRCHEARTFAILURE.120.006996.
36. Chen H, Deng Y, Gan X, Li Y, Huang W, Lu L, Wei L, Su L, Luo J, Zou B, Hong Y, Cao Y, Liu Y, Chi W (2020) NLRP12 collaborates with NLRP3 and NLRC4 to promote pyroptosis inducing ganglion cell death of acute glaucoma. Mol Neurodegener 15:26. https://doi.org/10.1186/s13024-020-00372-w.
37. Muendlein HI, Connolly WM, Leiriao J, Nolan MA, Judge J, Smirnova I, Batorsky R, Poltorak A (2025) TNF switches homeostatic efferocytosis to lytic caspase-8-dependent pyroptosis and IL-1β maturation. Sci Immunol 10:eadq0043. https://doi.org/10.1126/sciimmunol.adq0043.

# Figures

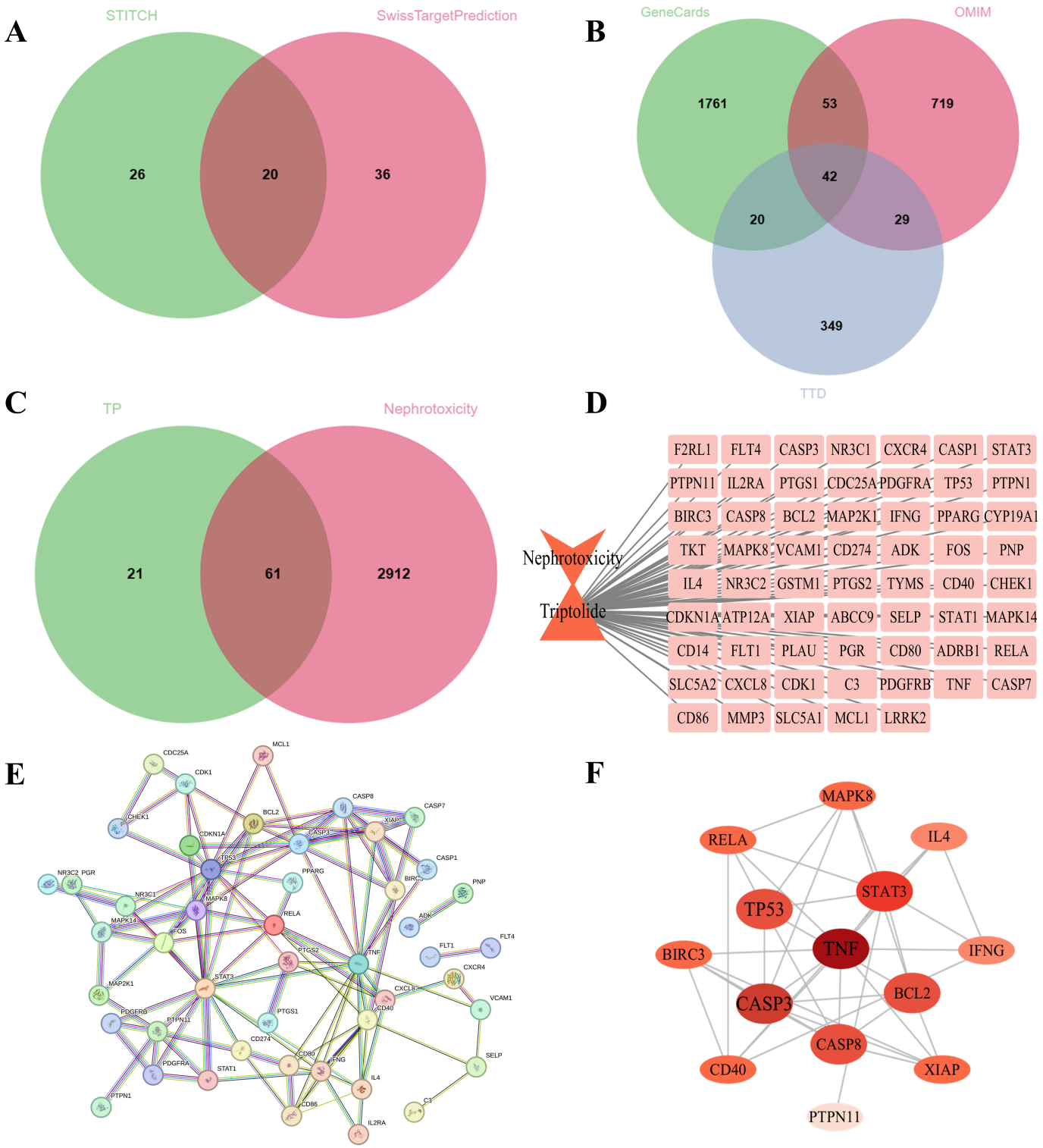
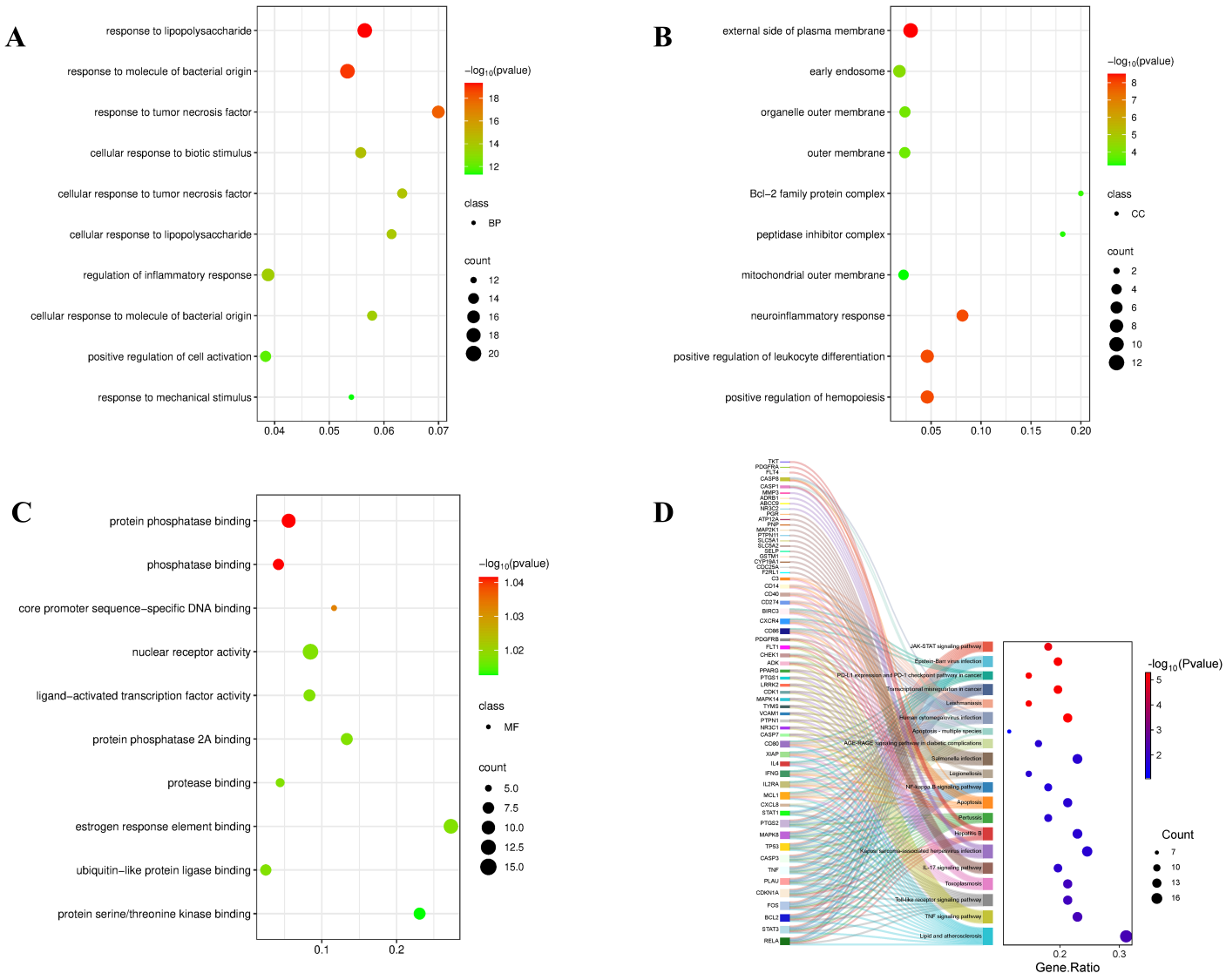


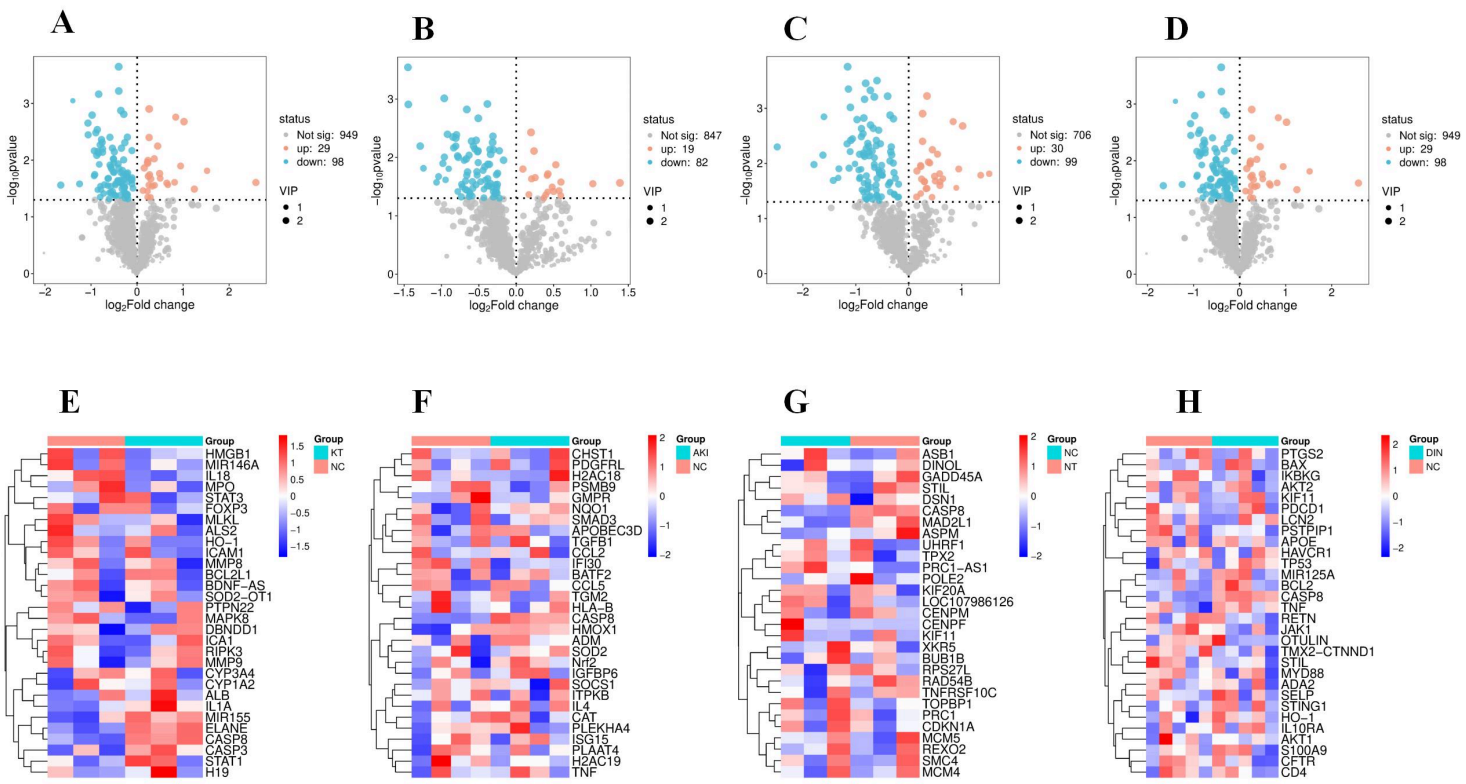

**Figure 1**

A–C: Venn diagrams, D: Target interaction network between TP and nephrotoxicity, E: PPI network, F: Regulatory network of core targets.



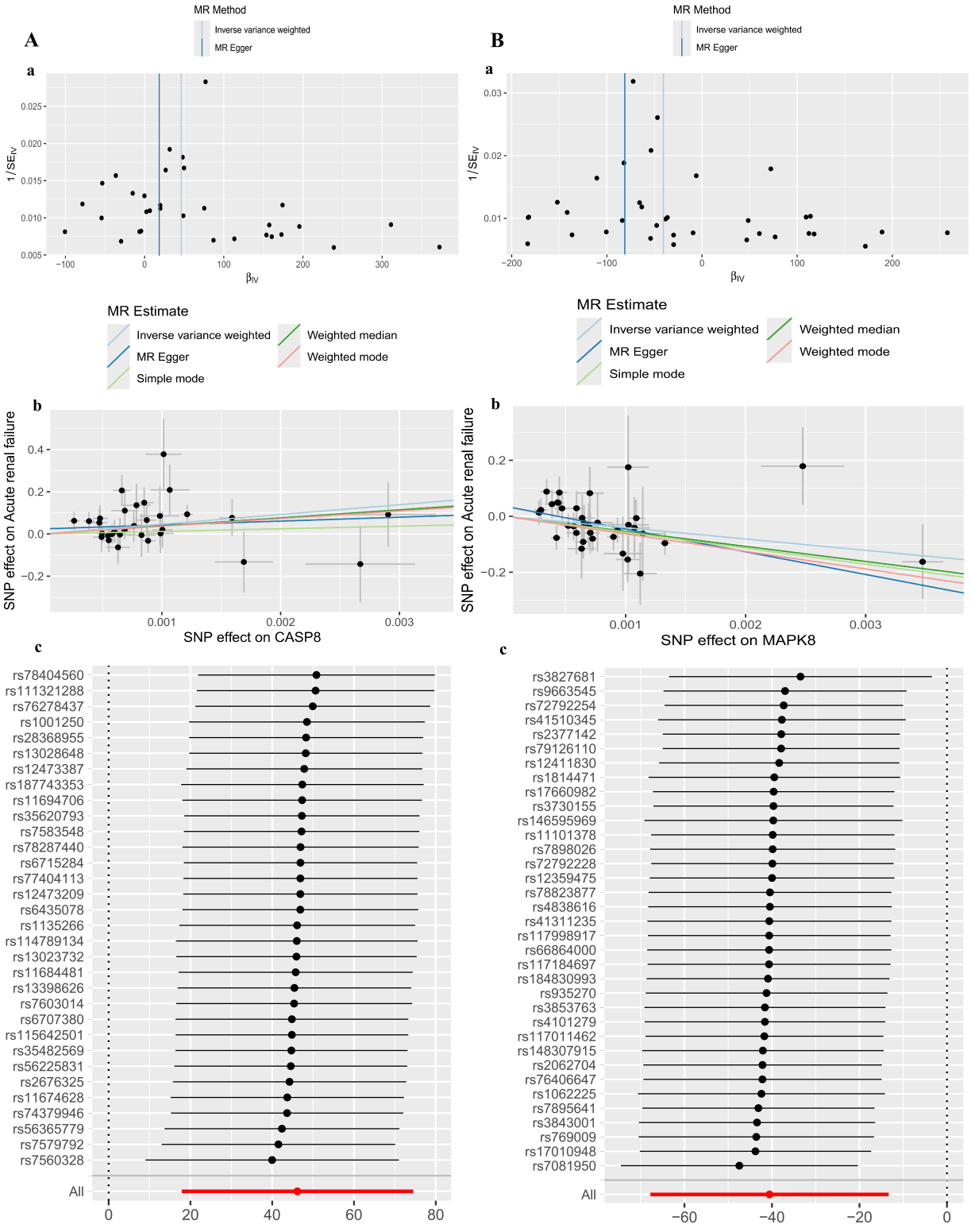

## Figure 2

A: BP enrichment analysis, B: CC enrichment analysis, C: MF enrichment analysis, D: KEGG Sankey diagram.



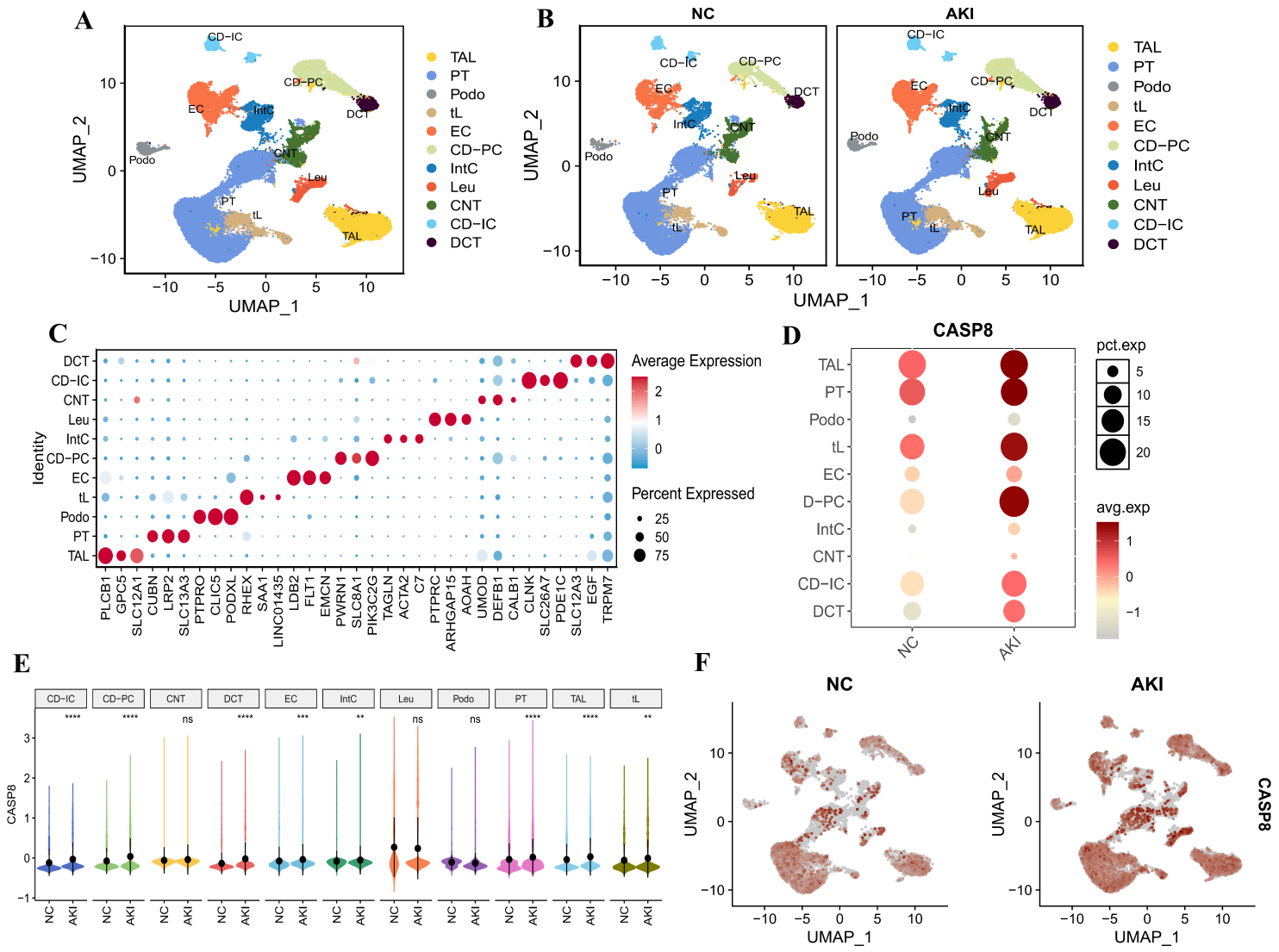

## Figure 3

Volcano plot and heatmap analyses of differentially expressed genes in Kidney Toxicity, Acute Kidney Injury, Nephrotoxicity, and Drug-induced Nephrotoxicity datasets (A–D: volcano plots; E–H: heatmaps).




## Figure 4

A: Mendelian randomization analysis results for CASP8 protein, B: Mendelian randomization analysis results for MAPK8 protein. a: Scatter plots showing the effects of individual SNPs on the exposure (protein levels) and the outcome (nephrotoxicity), b: Funnel plots, with different colored lines representing the five Mendelian randomization methods (IVW, MR-Egger, weighted median, weighted mode, and simple mode), c: Leave-one-out sensitivity analysis plots.




## Figure 5

A: UMAP of 11 renal cell populations, B: Grouped UMAP of NC and AKI, showing cell composition differences, C: Dot plot of marker genes confirming cell type annotation, D: Dot plot of CASP8 expression in NC/AKI renal cells, E: Violin plot of CASP8 differential expression in renal cells (NC vs AKI; ****$p$<0.0001, ***$p$<0.001, **$p$<0.01, ns: not significant), F: FeaturePlot of CASP8 in UMAP space (NC vs AKI), showing enrichment in proximal tubular and immune cells.

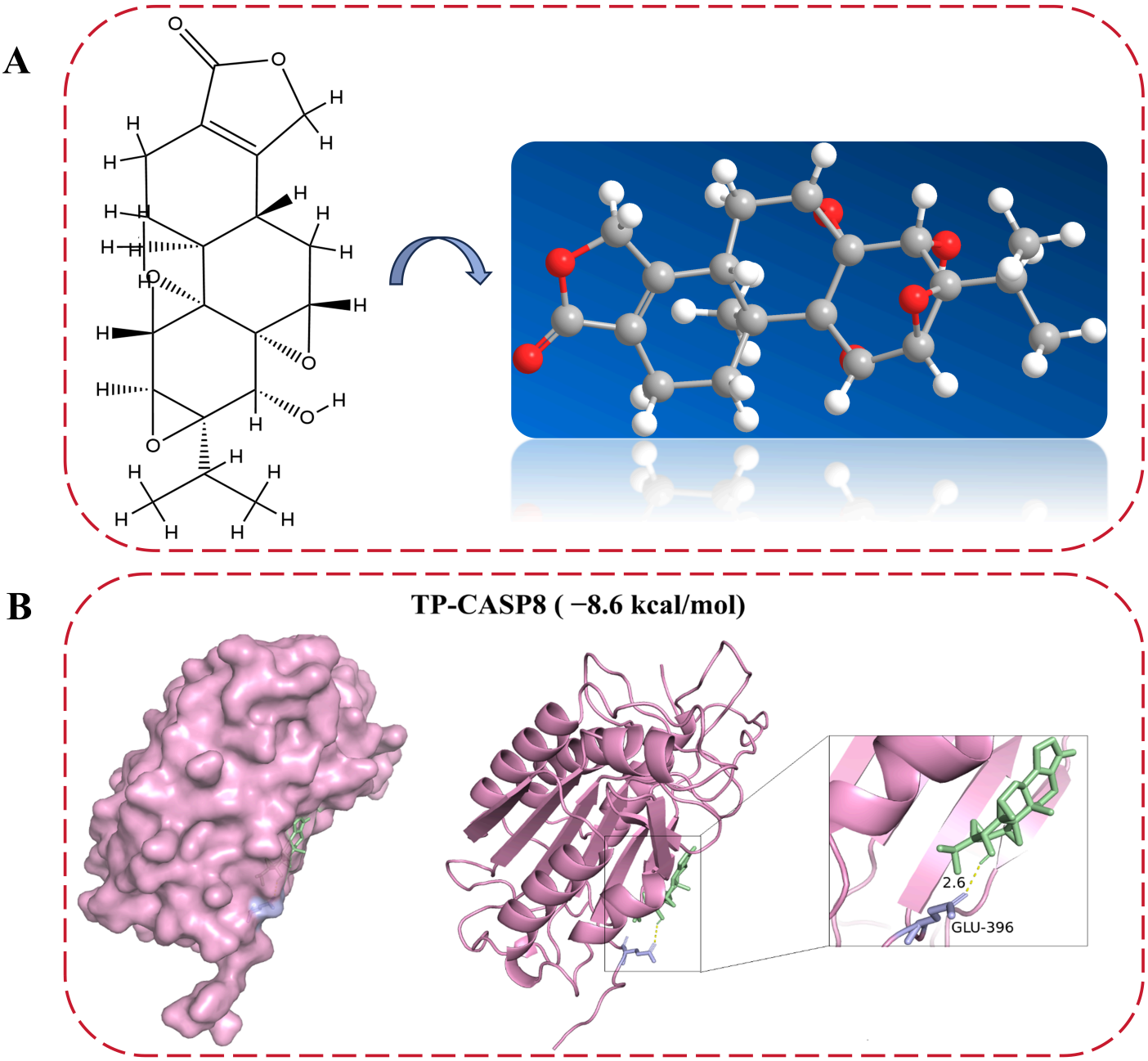
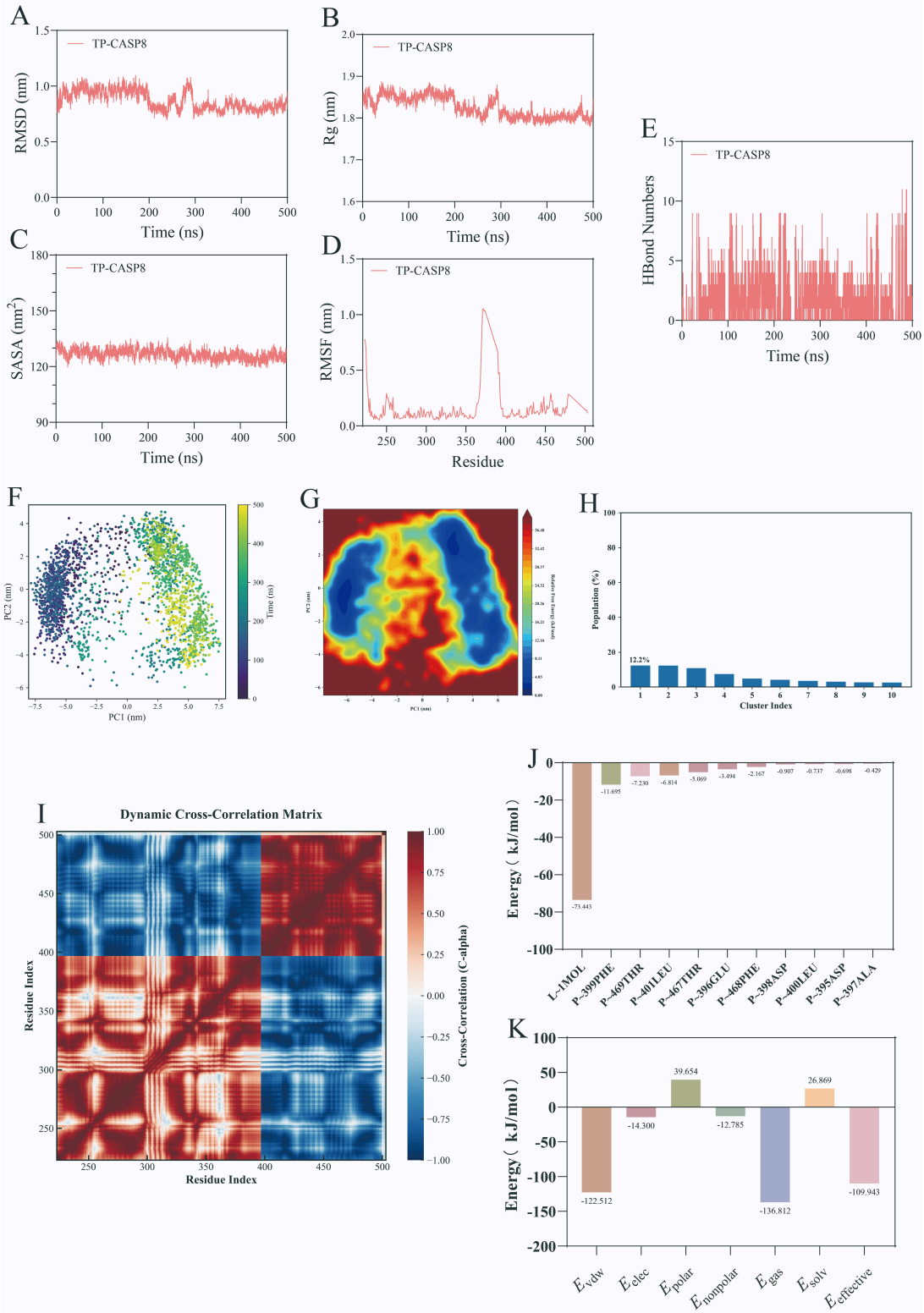



**Figure 6**

A:2D and 3D structures of TP, B: Overall structure of the TP–CASP8 complex and docking interactions.




## Figure 7

A: RMSD of the TP–CASP8 complex, B: Rg of the TP–CASP8 complex, C: SASA of the TP–CASP8 complex, D: RMSF of the TP–CASP8 complex, E: Number of hydrogen bonds in the TP–CASP8 complex, F: PCA scatter plot of the TP–CASP8 complex, G: Free energy landscape of the TP–CASP8 complex, H: Cluster index population analysis of the TP–CASP8 complex, I: Dynamic Cross-Correlation Matrix of the

TP–CASP8 complex, J: Energy decomposition of the system, K: Visualization of the total binding free energy and its energy components.